LANGMUIR

pubs.acs.org/Langmuir Article

Coupled Dynamics of Colloidal Nanoparticle Spreading and Self-Assembly at a Fluid-Fluid Interface

Daniel M. Balazs, Tyler A. Dunbar, Detlef-M. Smilgies, and Tobias Hanrath*



Cite This: Langmuir 2020, 36, 6106-6115



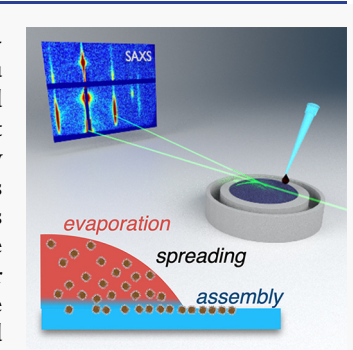
ACCESS

Metrics & More



SI Supporting Information

ABSTRACT: We investigated the physicochemical and transport phenomena governing the self-assembly of colloidal nanoparticles at the interface of two immiscible fluids. By combining in situ grazing-incidence small-angle X-ray scattering (GISAXS) with a temporal resolution of 200 ms and electron microscopy measurements, we gained new insights into the coupled effects of solvent spreading, nanoparticle assembly, and recession of the vapor—liquid interface on the morphology of the self-assembled thin films. We focus on oleate-passivated PbSe nanoparticles dispersed across an ethylene glycol subphase as a model system and demonstrate how solvent parameters such as surface tension, nanoparticle solubility, aromaticity, and polarity influence the mesoscale morphology of the nanoparticle superlattice. We discovered that a nanoparticle precursor monolayer film spreads in front of the bulk solution and influences the fluid spreading across the subphase. Improved understanding of the impact of kinetic phenomena (i.e., solvent spreading and evaporation) on the superlattice morphology is important to describe the formation mechanism and ultimately enable the assembly of high-quality superlattices with long-range order.



■ INTRODUCTION

The self-assembly of nanoparticles (NPs) into complex superstructures is of widespread scientific and technological interest for the prospect of creating materials whose properties and function can be tuned through the choice of and interaction between constituent particles. During the last decade, research into self-assembly has received a significant boost from the availability of high-fidelity colloidal NP building blocks with precisely engineered size, shape, and composition. Recent reviews have captured the exciting prospects of this emerging class of metamaterials in fields spanning catalysis, as well as electronic, thermoelectric, magnetic, and photovoltaic applications, revolutionizing energy material research.

In atomic crystals and self-assembled supercrystals alike, access to high-quality single crystals is a critical prerequisite to understanding their fundamental properties and enabling emerging technologies. Many of the challenges to assembling colloidal NPs into a well-defined "single crystal" superlattice derive from the complexity of the interactions between NPs and the interplay between different physicochemical and transport phenomena that occur during the assembly. 16-18 Fluid interfaces have emerged as a versatile and effective platform to direct the self-assembly of high-fidelity NP assemblies over large areas. 19-21 Moreover, the fluid substrate allows for chemical modification of the ligand shell of the selfassembled NPs, for example, by using additives in the subphase. These processing advances have opened an exciting new field of atomically oriented and fused NP superlattices as a step toward bottom-up designed functional materials.²²⁻²⁵ Whereas the majority of previous studies of molecules or NP

assembly at fluid interfaces have focused on monolayers (ML), $^{26-29}$ the understanding of droplet spreading and crystallization as a way to achieve and modify multilayer-ordered superlattices is scarce; with the results and discussion presented in this manuscript, we aim to address this knowledge gap.

The basic aspects of NP assembly at the interface of two immiscible fluids are schematically summarized in Figure 1. At first glance, the assembly process is ostensibly simple; however, further consideration reveals that the formation of the assembly involves a complex interplay of several coupled subprocesses, including the spreading of the colloidal solvent across the fluid interface, the evaporation of the solvent, and the recession of the fluid interface. During these processes, the NP solution undergoes a "phase transformation" of a colloidal NP "gas" to an ordered thin film at the liquid—liquid or liquid—air interface. Although the spreading process of liquids on solid and liquid substrates is fairly well understood from a macroscopic point of view, ³⁰ the dynamic local structure at the molecular/NP level has been difficult to study with suitable temporal and spatial resolutions.

The fast temporal resolution (200 ms) afforded by synchrotron-based in situ grazing-incidence small-angle X-ray

Received: February 24, 2020 Revised: April 21, 2020 Published: May 11, 2020





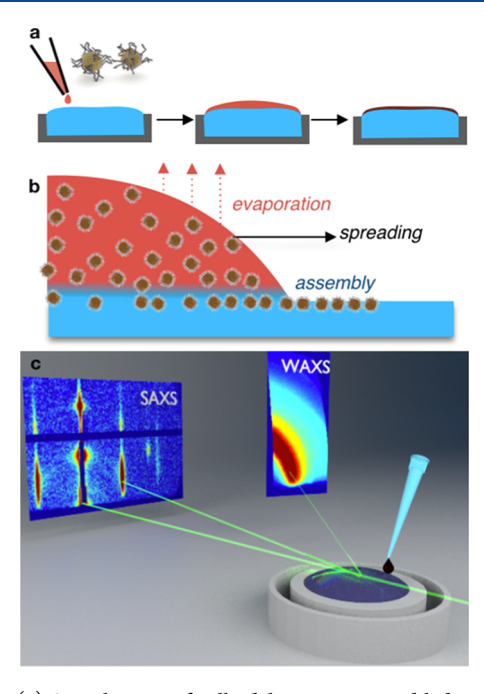


Figure 1. (a) Superlattices of colloidal NPs are assembled at a liquid—liquid interface by simple drying; (b) the spreading and drying processes, as well as the resulting structure, are studied using in situ synchrotron-based grazing-incidence small-angle X-ray scattering (GISAXS); and (c) sketch of the experimental system.

scattering (GISAXS) presents an opportunity to gain new insights into the dynamics of NP assembly at the interface between two immiscible fluids. We leveraged the fast temporal resolution to reveal the existence of a monolayer NP film rapidly spreading ahead of the "bulk" colloidal NP solution. This NP "precursor" monolayer has important implications on the spreading of the bulk solution and the formation of the NP multilayer assembly. We discuss differences in the spreading dynamics observed with different solvents in terms of the NP solubility and wetting properties, and relate the initial dynamics to the final structure of the NP assembly. Analyzing and comparing the fluid-phase and the superlattice-phase scattering signals allowed us to study the superlattice formation throughout the assembly process.

METHODS

NP Synthesis. PbSe NPs were prepared by the method reported following literature recipes. ^{24,31} The synthesis was carried out in a three-necked flask under an inert nitrogen atmosphere. First, PbO (4 mmol, 0.892 g) and oleic acid (~10 mmol, 3.2 mL) were dissolved in 1-octadecene (ODE, 15.5 mL) to yield a precursor solution. The solution was then degassed by heating stepwise to 110 °C over the course of 1 h under <10 Pa vacuum, after which the flask was filled with nitrogen from the well-flushed Schlenk-line, and the solution was heated to 160 °C. In a glovebox, Se was dissolved in trioctylphosphine (TOP) to yield a 1.67 M stock solution. Next, diphenylphospine (DPP) was added to the TOPSe solution at a final concentration of 0.1 M. Seven milliliters of the TOP/DPP-Se solution was rapidly injected into the vigorously stirred, hot lead oleate solution. PbSe NPs formed immediately after injection, the temperature dropped to about 145 °C, and the crystal growth was allowed to proceed for 3 min, when the reaction was quenched by removing the heating mantle, injecting a 1:1 volume toluene, and placing the bottle in a water bath. Following the synthesis, the NPs were washed several times by sequential precipitation with acetone and redispersion in toluene. Based on the statistical analysis of transmission electron microscopy (TEM) images and UV-vis characterization, the PbSe NP cores had

an average diameter of 6 nm with a 5% relative size distribution. The NPs were kept in toluene in the glovebox, dried, and redispersed in the desired solvent for superlattice formation.

UV–Vis Spectroscopy. Spectra (Figure S1) were taken from dilute solutions in tetrachloroethylene using a Cary 5000 spectrometer. The size and concentration were extracted following the work of Moreels et al.³²

TEM Analysis. Transmission electron microscope (TEM) imaging was performed with an FEI Tecnai T12 operated at a 120 keV accelerating voltage equipped with a LaB_6 filament and a top-mount SIS Megaview II camera. Samples of the dry film were collected from the ethylene glycol (EG) surface by the Langmuir—Schaefer method and dried in vacuum before imaging.

NP Superlattice Formation. The superlattice formation was performed by dropping a low-volume (1 μ L), high-concentration (0.18 mM, \sim 130 mg/mL) NP solution onto the flat surface of 4 mL EG contained in a round poly(tetrafluoroethylene) (PTFE) trough with 4.3 cm diameter mounted at the X-ray beam path. The NP solution was introduced as a droplet suspended from a syringe needle, brought into contact with the EG subphase using a remote-controlled manipulator. The droplet of the NP solution was added \sim 1.5 cm from the beam path to capture the entire spreading process.

X-ray Scattering Characterization. Grazing-incidence smallangle X-ray scattering (GISAXS) measurements were performed at beamline D1 of the Cornell High Energy Synchrotron Source (CHESS) using a monochromatic radiation of wavelength $\lambda = 1.162$ Å with a bandwidth $\Delta \lambda/\lambda$ of 1.5%. The X-ray beam was produced by a hard-bent dipole magnet of the Cornell storage ring and monochromatized with Mo/B₄C synthetic multilayers with a period of 30 Å. Small-angle scattering data was obtained using a Pilatus 200k air-cooled pixel array detector with a pixel size of 172 μ m \times 172 μ m and a total of 487 × 407 pixels with a 32-bit dynamical range per pixel. Wide-angle scattering data was obtained using a Pilatus 100k detector with similar specifications but 487 × 195 pixels. The sampleto-detector distance was 1307 mm, as determined using a silver behenate powder standard with in-house software GIXSpack. The incident angle of the X-ray beam was 0.25°, between the critical angles of the EG subphase and the PbSe NP material. Image series of 150 frames with 0.2 s integration per frame were recorded during the spreading process; this 30 s window allowed the samples to fully dry. Scattering images were indexed, integrated, fitted, and simulated using purpose-built MATLAB scripts or GIXSGUI.³³

During postprocessing of the X-ray scattering data, we sought to model interparticle interactions in both the liquid and superlattice phases. The colloidal gas/liquid phase was modeled using the Baxter Adhesive sphere model, in which the NPs have an attractive square-well potential with width Δ and depth u_o . A u_o , and particle volume fraction, ϕ , as unknown parameters. The well width was treated as the ensemble-average length of ligand extension from the NP surfaces. The superlattice spacing between particles, or "effective diameter", was determined from the inverse of the Bragg peak location along q_x . Further details of the analysis and the underlying theory are discussed in the Supporting Information (SI).

■ RESULTS AND DISCUSSION

We performed the self-assembly experiments using oleate-capped, 6.1 nm PbSe NPs with $\sim 5\%$ polydispersity (see the details in the Methods section and the Supporting Information). Aliphatic solvents such as hexane and octane are among the most commonly used solvents for interfacial assembly of such colloidal NPs due to their low viscosity, surface tension, and low miscibility with EG as the polar subphase. For practical purposes, we sought to replace the conventional low-boiling solvents like hexane with less volatile solvents to slow down the evaporation without the need for a controlled vapor atmosphere in a closed chamber. We selected three solvents with similar boiling points and molecular

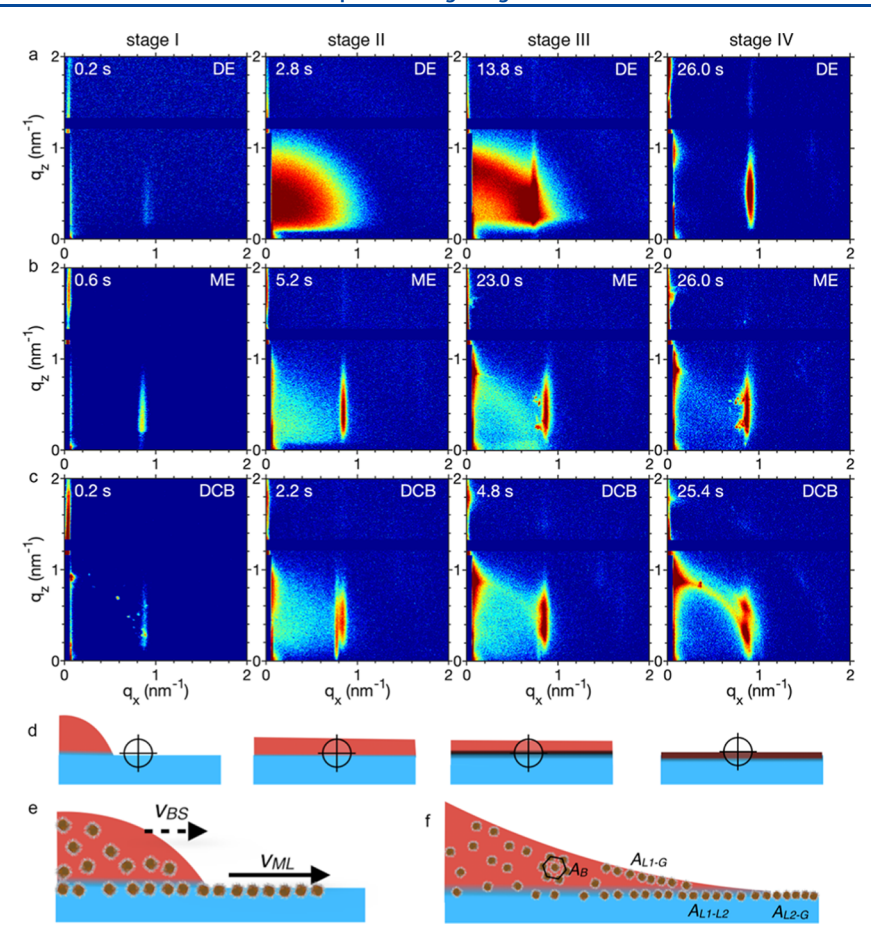


Figure 2. Temporal dynamics of the superlattice formation from the droplet to the superlattice using (a) decane, (b) mesitylene, and (c) dichlorobenzene captured using GISAXS. The snapshots are taken before the droplet spreads across the beam path showing the precursor monolayer (stage I), after the droplet spreads across the beam path showing a pure solution or coexisting monolayer and solution (stage II), before the crystallization showing the intermediate structures (stage III), and after visibly complete drying (stage IV). The color scales in (a)—(c) are correlated to the intensity data on the logarithmic scale. (d) Sketches of the corresponding phenomena, with the crosshair representing the X-ray beam location. (e) Schematic illustration of the relative spreading velocity of the "bulk solution" and the faster NP monolayer. (f) Schematic illustration of the densification of the NP solution during solvent evaporation and formation of assemblies within the bulk (not observed) and fluid interfaces.

weights that exhibit similar volatility but decreasing NP solubility as listed: decane (DE), mesitylene (ME), and dichlorobenzene (DCB). The differences between the solvents lie in their physicochemical properties: DE is apolar and aliphatic, ME is apolar and aromatic, and DCB is polar and aromatic. We define the NP solubility limit as the maximum concentration at which the colloidal dispersion is stable; at NP concentrations above the solubility limit, the NP dispersion leads to agglomeration and superlattice formation as detailed below. Hansen solubility parameters (HSPs) of the solvents, as well as those of EG, are provided in the Supporting Information, together with a relative energy density estimate.³⁶ DE and ME are expected to be immiscible with EG, whereas DCB is on the verge of miscibility. The oleate-passivated PbSe NPs have notably different solubilities in each of the solvents. DE and ME are "good" solvents in terms of "solvent quality": DE disperses NPs at high concentrations immediately, ME shows slower dispersion times and is expected to lead to lower solubility than alkanes, while DCB requires time to dissolve the NPs at high concentration, and the applied concentration approaches the saturation level.^{37,38} We estimated the HSP of the oleate-passivated NPs using various solvents, and the

calculated solubility in these solvents matches the observations (see the Supporting Information).

The spreading and drying dynamics of NP solutions in DE, ME, and DCB show profoundly different behavior. Videos taken from the spreading and drying processes (see in the online SI and Figures S2 and S3) confirm that the three solvents evaporate slow enough (10-30 s) for practical purposes. The DE solution spreads completely (from the inside out) and dries in an orderly fashion (inward from the edges of the trough), with a contact line velocity of ~ 1 mm/s (Figure S3a). The ME solution also spreads well initially, but the spreading stops before the bulk droplet reaches the edge of the trough, and a thin film is formed around the edges. The droplet then starts to withdraw slowly, which leaves behind a thicker film, with a contact line velocity similar to that using DE. At the end, however, signs of partial wetting are observed and the remainder of the ME solution forms droplets in the center of the trough, surrounded by the solid film. The spreading behavior of the DCB solution is markedly different from that of DE and ME. Soon after depositing the DCB solution onto the EG subphase, the DCB disappears, while small droplets containing most of the NPs are formed. We attribute this behavior to the partial miscibility of DCB in EG.

All three solvents create areas that are macroscopically homogeneous. To understand how these solvent characteristics and the spreading behavior impact the NP superlattice formation, we studied the three systems using time-resolved X-ray scattering throughout the spreading and drying processes.

The general approach and the experimental design are shown in Figure 1. Briefly, NPs dispersed in a solvent were dropped onto an essentially flat ethylene glycol (EG) liquid reservoir (the subphase) at ~1.5 cm from the X-ray beam path, and GISAXS and grazing-incidence wide-angle scattering (GIWAXS) patterns were recorded with a high temporal resolution (200 ms) to examine the evolution of the film structure during subsequent spreading and drying of the NP solution. We note that X-ray scattering at wide angles was dominated by ring-like features, indicating that the colloidal NPs did not exhibit a preferential orientation relative to the interface during the initial spreading and assembly phases of the experiment (shown in Figure S12).

Figure 2 summarizes the GISAXS data acquired during the assembly of colloidal PbSe NP solutions in various solvents. We first discuss the main features observed in the assembly experiments with NPs dispersed in DE (Figure 2a) and then compare the significant differences observed in ME (Figure 2b) and DCB (Figure 2c). Figure 2d—f provides an illustrative interpretation of the key structural features observed during the experiment.

Immediately after the droplet of NP solution contacts the EG subphase (stage I), weak Bragg peaks are observed near q_x ~ 0.9 nm⁻¹; these correspond to an ordered thin NP film at the interface (Figure 2, left column). The out-of-plane scattering signature suggests the presence of a densely packed NP monolayer (see the extracted profiles in Figure S4), which spreads rapidly ahead of the bulk solution, as schematically illustrated in Figure 2e. This phenomenon is known as the "precursor film" in the classical wetting theory, a "molecular" film bridging the interfacial energy discontinuity at the contact line. 30,39 Although the dynamics in liquids spreading on liquids is slightly different, precursor films have also been indirectly observed during the spreading of surfactants on water: a droplet of two species with different interactions with the subphase will partition, and the favored species will dominate the forward-moving edge to form the precursor film.⁴⁰

Within the first 2-5 s (stage II), the bulk NP solution in DE spreads across the beam path, as indicated by the blob-like scattering pattern. The spreading DE solution fully dissolves the precursor film (in agreement with the visual observations of the droplet covering the entire trough). In dilute solutions, the NPs are uncorrelated (i.e., a colloidal gas), and the scattering pattern reflects the form factor of the NPs. We fit the dilute scattering pattern (such as the one in the second column of Figure 2a) to a theoretical model of a spherical NP to determine a mean particle diameter of 6.1 nm with a polydispersity of 8% (see Figure S6), 24,43 which is consistent with the size and polydispersity obtained from UV-vis spectroscopy of 6.1 nm and 5.5%, respectively (see Figure S1).³² The deviation in polydispersity is most likely caused by the Vineyard factor not being included in the form factor calculation.43

As the solvent evaporates, the NP concentration within the thin liquid film gradually increases, which leads to a phase transition from the initial NP colloidal gas to a dense liquid to a network of solvated but correlated NPs and ultimately an ordered assembly (i.e., solid). These transitions can be tracked based on the X-ray scattering signature of the film. The blob-like features creep outward from the reflected beam origin to form rings indicating a transition to a dense NP solution. ^{34,44} During this time period, we also observe temporary superlattices with different spacings (multiple peaks in proximity; see Figure S9).

Upon further evaporation of the solvent, the NP concentration gradually increases to the point at which scattering signatures of superlattice crystallization are observed (stage III). The dense fluid scattering and superlattice scattering rods are observed simultaneously but only for less than a second. This scattering signature is likely due to the rather long grazing beam path interacting with the interface (23 mm at 0.25° incidence covering an area of ~10 mm² across the trough); both the dry and the wet areas are tested for a short period. When at last all of the solvent is evaporated (stage IV), strong scattering rods are observed. Complete NP superlattice crystallization in the beam path occurs over ~5 s (see the videos in the SI; snapshots not shown), resulting in an face-centered cubic (fcc)-like superlattice with its densely packed {111}-equivalent hexagonal plane aligned to the fluid interface. This structure is confirmed by the presence of (11) and (20) scattering rods of the hexagonal plane that are, respectively, ~ 1.7 and 2 times larger than the q_x value of the first-order (10) in-plane peak and the characteristic out-ofplane pattern of the (11) rods. 43 The broad peak at relatively high q_z values in the (10) scattering rod (Figure S4) suggests a mixed system, with the presence of both hexagonal closepacked (hcp)- and fcc-type stackings of the hexagonal planes (ABA and ABC types considering the NP positions). Bulk crystal indexing of the patterns focusing on the (00) and (11) rods (that are less affected by stacking faults) suggests an ~5% out-of-plane shrinkage (see Figure S5).⁴³ Moreover, some of the replicate samples show a distortion from the hexagonal inplane symmetry in line with the previous observations of bodycentered cubic (bcc), tetragonal, or rhombohedral phases.⁴⁵

In the case of NP solutions in ME, scattering patterns acquired within the first second show clear signatures of the rapidly spreading NP monolayer precursor film (left column, Figure 2b). Interestingly, the scattering intensity of the NP monolayer precursor film is more pronounced compared to those observed in NP solutions in DE. We have compared the experimental scattering patterns to simulated patterns to confirm that the precursor film observed in ME experiments is a dense NP monolayer (see the out-of-plane profile in Figure S4). In later stages of the spreading and drying (i.e., stages II and III), a thick (2-3 monolayer) superlattice phase similar to that observed using DE coexists with the bulk solution. The shape of the superlattice scattering signatures is unaffected by the drying process, which suggests that the film thicknesses are effectively constant (see Figure S4) and consequently that the surface areas corresponding to the precursor film (monolayer), self-assembled superlattice, and receding liquid are laterally separated. These distinct regions are also clearly visible in the photograph in Figure S3.

In the final stage of the process (i.e., stage IV), the scattering signatures of the films show dominant peaks of a thick fcc lattice superposed onto the previously existing superlattice profile. We attribute these scattering signatures to the NP superlattice crystallization driven by the drying of the confined, concentrated NP solution droplets observed in the videos. Moreover, a set of sharp spots near the main superlattice

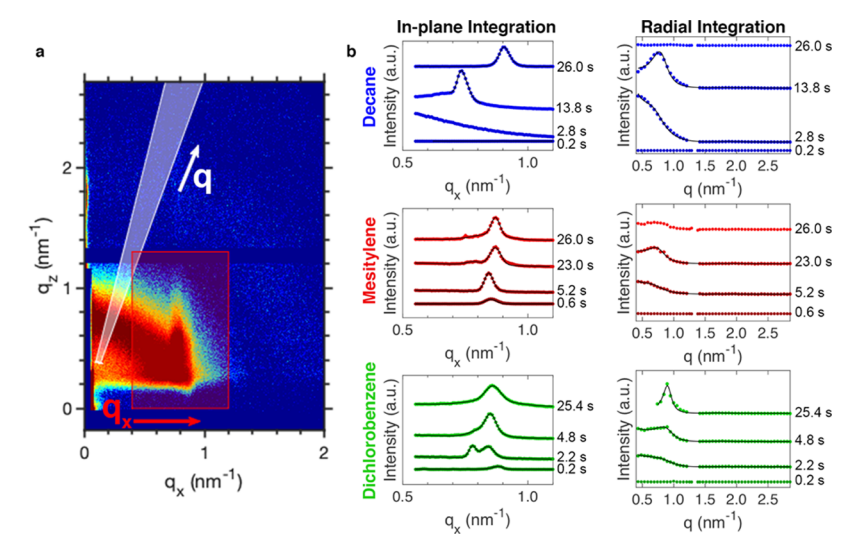


Figure 3. Quantitative analysis of the in situ X-ray scattering data: (a) integration ranges for radial (white shading) and in-plane (red shading) intensity profiles and (b) in-plane (left column) and radial (right column) integration profiles over the temporal regimes indicated in Figure 2 for DE, ME, and DCB, respectively. The black lines for the in-plane integrations show fits to the Bragg peaks, and for radial integrations, they indicate fluid-phase scattering fits for curves with a sufficient signal-to-noise ratio.

scattering rods appear at the final stage of the drying. These spots may be related to larger, well-ordered crystallites in the beam path, with lattice spacing larger than the main superlattice (likely due to the remnant solvent).

Experiments using NPs suspended in DCB reveal several additional scattering features not observed with DE or ME (Figure 2c). One notable difference is that the morphology of the final film (stage IV, the right column of Figure 2c) also includes a powder-like diffraction ring. This scattering signature indicates the presence of NP assemblies that are randomly oriented relative to the substrate (similar to a powder diffraction pattern) or a glassy phase with only shortrange translational and no rotational order. The lack of higherorder rings suggests that we observe a glassy phase; however, the data is not conclusive as the NP form factor can suppress the scattering signal at higher q-values. The lack of preferential orientation suggests that either the glassy or bulk crystal assemblies may have formed in the bulk solution (denoted as $A_{\rm B}$ in Figure 2f). We note that the formation of threedimensional (3D) NP assemblies in the "bulk fluid" can be ruled out in DE and ME based on the absence of the ringscattering pattern. The second panel in Figure 2c, at t = 2.2 s (stage II), reveals a transient double-scattering rod, which exists for up to 5 s during the transition from a dense liquid to a dry superlattice. The second peak indicates a second in-plane crystalline phase with a larger lattice spacing than the first phase. We have considered two possible interpretations of this dual structure. One hypothesis is that the two scattering signatures arise from assemblies formed at both the liquidliquid and liquid-gas interfaces as illustrated by A_{L1-G} and A_{L1-L2} in Figure 2f. The alternate hypothesis is that the two scattering signatures arise from multiple grains arranged laterally across the X-ray beam path, with one set of grains more solvated by the solvent than the other set. The previously discussed presence of both dry and wet areas in assemblies formed from NP solutions in ME and inhomogeneous drying in the beam path favor the second interpretation of two laterally separated, transient crystalline phases, one containing more remaining solvent as the temporary spacer. Interestingly, the transient double reflection is also observed for NP

dispersed in DE and ME, albeit the coexistence is limited to less than a second for DE and around 3 s for ME (Figure S9). The presence of a broad second peak has been assigned to areas of a monolayer particulate film showing a two-dimensional (2D) glassy phase; however, our sharp peaks suggest a well-defined crystalline phase similar to the final one.⁴⁸

Beyond a qualitative comparison of the transient processes described above, the rich information content of the X-ray scattering data also provides important quantitative insights. Two variables of particular interest include the effective diameter of the colloidal NP and the volume fraction of the solution. The effective particle diameter reflects the extent to which the dispersing solvent swells the organic ligand shell surrounding the NP core. Since the diameter of the inorganic NP core is the same in our experiments, the effective diameter determined from X-ray scattering experiments thus reflects the "softness" of the colloidal NP dissolved in various solvents. The NP volume fraction provides an important metric in the phase transition from colloidal gas to dense liquid and ultimately to the NP superlattice (colloidal solid). We extracted the effective diameter of the NPs in both the fluid and the superlattice phases as follows. For the superlattice phase, we determined the in-plane positions of the first-order Bragg peaks (both peaks in the case of peak splitting) and converted them to real-space distances assuming a hexagonal symmetry and used these nearest-neighbor distances as the effective diameter of the particles in the superlattice phase. For the liquid phase, we extracted the radial intensity distribution at a q-range that does not overlap with any of the out-of-plane scattering rods and fitted a simulated curve describing the fluid-phase scattering pattern based on the work of Baxter (see Figure 3a). 34,49 We modeled the fluid phase using a square-well attractive potential, with independent parameters being the volume fraction of the scatterers, the correlation length (the nearest observed center-to-center distance possible in the system), and the strength of interaction between particles. We consider the correlation length as the effective NP diameter in solution and use the volume fraction to track the solvent loss. Figure 3 shows the in-plane and radial integration ranges,

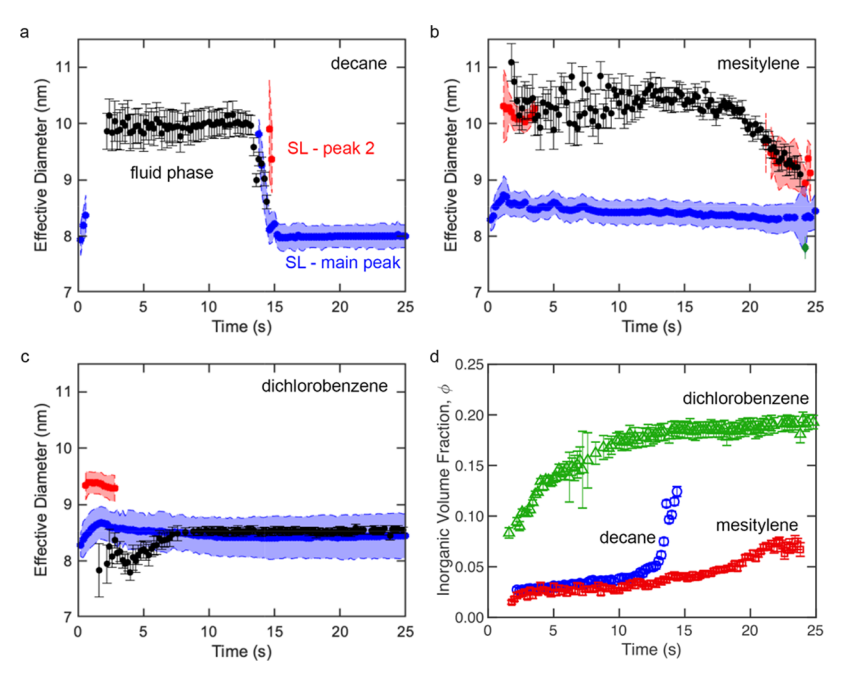


Figure 4. Effective NP diameter in the fluid phase (black markers) and in the 2D crystalline phase (blue and red markers for first and intermittent second peaks) for experiments using (a) DE, (b) ME, and (c) DCB as solvents. (d) NP volume fraction in the fluid phase determined from Baxter fits. Error bars represent the 95% confidence interval of the Baxter fits, and shaded regions of the effective diameter plots indicate the full width at half-maximum of the solid-phase Bragg peaks.

extracted intensity data, and best-fit curves for each panel in Figure 2. Additional details of the quantitative analysis and modeling are discussed in the Methods section and the Supporting Information.

The fitted values for the fluid- and superlattice-phase effective diameters and NP volume fractions are shown in Figure 4 for all three NP solutions. Fits were attempted for each recorded frame during the 25 s collection period, but only those with reliable fit are shown. The error bars represent the confidence interval of the fit (fluid-phase) and the peak width (superlattice phase). During the early stages of the experiment, the fluid-phase fit involves a relatively high uncertainty in the effective diameter; at later stages, this high uncertainty decreases because of an increasing dependence on the structure factor (which is a function of the effective diameter). As the colloidal solution densifies, the structure effects have more impact on the intensity profile, which in turn reduces the uncertainty of the fit.

The effective diameter at early times (stage I) corresponding to the NPs in the precursor monolayer shows similar nearestneighbor spacing to the final (stage IV) superlattice (see the blue markers in Figure 4a-c), indicating its dense, almost solvent-less nature. The effective diameter in these initial films increases with time in the case of all three solutions, which suggests a gradual swelling of the NP ligand shell as the solvent follows the solute precursor film into the path of the X-ray beam. In the case of NP solutions in DE, the solvent redisperses the NPs rapidly and completely. By contrast, in the cases of ME and DCB, the Bragg peaks of the ordered NP precursor monolayer persist and the solution phase and monolayer scattering signals superpose. These observations can be correlated to the videos; the beam path covering both dry and wet regions explains the coexisting features. While precursor films on solid substrates and static structures at the liquid—liquid interfaces have been studied using various methods, 30,50,51 the understanding of the dynamic phenomena on liquid surfaces is limited by the lack of available techniques due to the high spreading velocity and geometric constraints. The continuous development of high-speed X-ray detectors and bright light sources has promise for reopening the field to new mechanistic studies.

During stage II, the fluid-phase effective diameters of the colloidal NPs are ~10 nm in DE, ~10.5 nm in ME, and ~8.5 nm in DCB (see the black markers in Figure 4a-c). The slight difference in the effective NP diameters between DE and ME is due to minor differences in NP size and ligand coverage; the NPs used for the DE experiment were synthesized separately from the NPs used for ME and DCB with nearly identical size distributions. To underscore the reproducibility of the trends shown in Figure 4, we provide an additional in situ experiment for DE using the same NPs as ME and DCB in the SI. The 10 nm effective NP diameter is consistent with the simple model of an ~6 nm inorganic NP core surrounded by an ~2 nm thick oleate ligand shell. This observation suggests that the ligand corona is swollen by the solvent in DE and ME, confirming the good solvent quality and the "soft" nature of the colloidal NP. The much shorter correlation length of NPs dispersed in DCB suggests a dense, collapsed ligand corona caused by the preferential ligand-ligand over ligand-solvent interactions. NPs dissolved in DCB are therefore characterized by a relatively harder colloidal interaction potential compared to the soft colloidal NP in DE and ME. These trends are consistent with the HSPs of the ligand and the solvents discussed earlier and in the SI.

Transient X-ray scattering patterns also provide insights into the evolution of the NP volume fraction during the spreading and superlattice formation. Initially, both DE and ME in Figure 4d show a steady increase in the inorganic NP core volume fraction in the fluid phase starting at close to the ~2% value calculated for the stock solution (~130 mg/mL, 0.18 mM). The initial increase in the volume fraction is comparable for DE and ME since the solvent is evaporating uniformly from

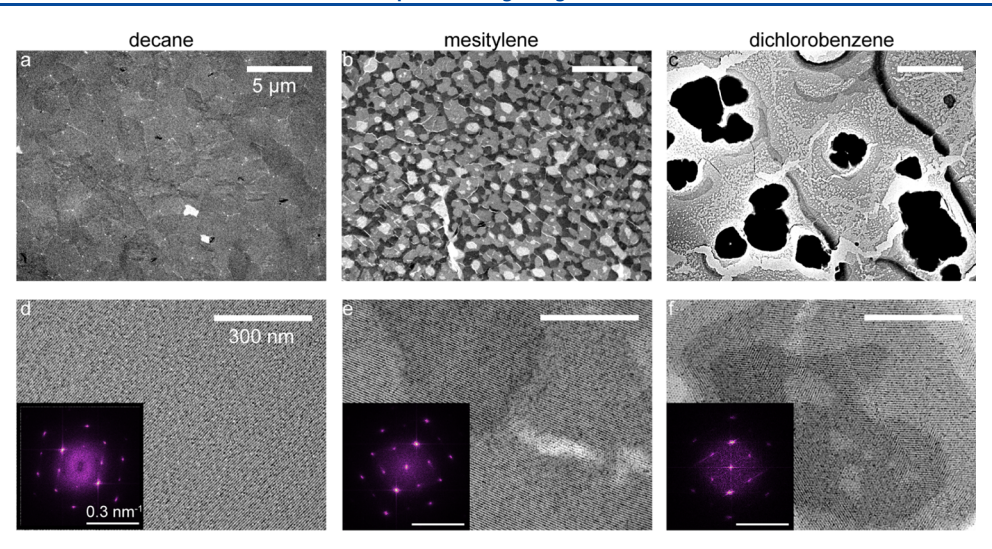


Figure 5. TEM images of the superlattices transferred to carbon grids at (a-c) low magnification showing the microscopic film morphology and (d-f) high magnification showing the nanostructure, using DE, ME, and DCB, respectively. The insets are the Fourier transform versions of the corresponding images showing a structure close to a $\langle 110 \rangle$ -oriented bcc lattice.

the surface of the exposed film. After approximately 12-15 s, the film prepared from DE solutions undergoes a rapid densification indicated by a sharp rise in the inorganic volume fraction (Figure 4c) and a decrease of the fluid-phase effective NP diameter (Figure 4a). This change overlaps in time with the appearance and contraction of a superlattice phase, and the effective diameters are strikingly similar in the two phases. The last observable fluid-phase effective diameters (before full drying) match those calculated from the temporary second Bragg peaks (secondary superlattice phases). The macroscopically observed contact line motion during drying (\sim 0.5 mm/s) and the width of the beam (~ 0.5 mm) give a transition time comparable to that observed from the volume fraction plot (<2 s), suggesting that the crystallization is mainly occurring at the contact line. In the context of the underlying phase transition, it is interesting to note that the maximum volume fraction matches the value corresponding to the onset of the Kirkwood-Alder transition if fully stretched ligands are considered ($\phi = 0.12 \times (10/6)^3 \sim 0.5$).⁵²

The inorganic volume fraction of NPs in films prepared from ME solutions increases more gradually up to an inorganic volume fraction of ~0.08, and full densification only occurs around 24 s. The effective diameter of NPs in ME (Figure 4b) starts to decrease well before full drying and also approaches the value calculated from the transient Bragg peak, slightly higher than the value obtained from the permanent superlattice phase. The lower final volume fraction (Figure 4d) of NP in ME compared to that in DE suggests that the superlattice phase develops from a less-dense fluid phase due to more favored ligand—ligand interactions compared to the solution in DE. The slower evaporation and densification in the case of ME solutions are likely due to the lower surface area of the contracted droplets.

The analysis of NPs dispersed in DCB reveals two notable differences. First, the initial inorganic volume fraction is higher than for DE or ME or the initial solution. The higher volume fraction (i.e., faster enrichment in the NP concentration) in DCB is likely the result of the loss of some DCB solvent to the EG subphase due to the partial miscibility of the solvent and subphase. Second, the effective diameter of the fluid and superlattice phases is identical after about 6 s, confirming that

the permanent scattering ring is actually a densely packed glassy phase with the same nearest-neighbor distance as in the superlattice (this analysis is more reliable than just qualitative assessment of the patterns discussed earlier as the form factor is fully included). The final inorganic volume fraction of \sim 0.19 (ϕ = 0.19 × (8.5/6)³ \sim 0.54 when the ligand shell is included) suggests that the NPs froze into a metastable loosely packed phase through the Kirkwood–Alder transition and did not complete the crystallization observed using DE and ME. Salthough it appears that there is an offset in the final superlattice spacing between DE, ME, and DCB, we do not consider it a significant trend as the sample-to-sample and spot-to-spot differences can cause an error of up to 0.2 nm.

To complement the X-ray scattering structure analysis, we also examined the micro- and nanoscale morphologies of similarly prepared samples using transmission electron microscopy (TEM) (Figure 5). The low-magnification images (Figure 5a-c) show that at micrometer length scales, NP assemblies formed from DE, ME, and DCB solvents show strikingly different morphologies. Films prepared from DE solutions yield a relatively uniform (3–4 NP monolayer thick) superlattice with a typical grain size on the order of $2-3 \mu m$. NP films formed from ME solutions show considerable thickness variations from 1 to 3-4 NP monolayers and slightly smaller grain sizes of about 1 μ m. The DCB samples show large aggregates of NPs surrounded by 1-2 monolayer thick, rather disordered films. The morphological differences evident from the TEM images can also be correlated to the out-of-plane X-ray scattering variation of the Bragg peaks, as detailed in the Supporting Information, Section 6.1.

Despite the above-mentioned differences in micrometer morphology and film formation dynamics, the nanoscale structures of the DE, ME, and DCB samples are remarkably similar, as illustrated by the high-resolution TEM images (Figure 5d–f). Fast Fourier transform (FFT) analysis of the superlattice structures in all samples reveals in-plane lattice vector angles of around 70–72°, matching that of a {110} surface normal-oriented bcc superlattice, with nearest-neighbor spacings between 8.2 and 8.4 nm. Whereas the NP superlattice structure formed on a fluid surface (e.g., EG) immediately after solvent evaporation is characterized by fcc, the NP films

imaged in the TEM are best described as a bcc-like lattice. Comparing the superlattice structures analyzed by GISAXS and TEM involves subtle differences, which are detailed in the Supporting Information, Section 6.2. The similarities in lattice spacing and symmetry suggest that the NP superlattice structure does not depend on the ligand shell solvation before self-assembly and the ligand corona is sufficiently flexible to find the thermodynamically favored configuration in the ordered phase (entropically driven Kirkwood–Alder transition).^{3,54}

To understand the relationship between the NP solvent and film morphology, we have to consider the interplay between several coupled processes, including the (i) initial rapid spreading of the NP precursor monolayer, (ii) spreading of the bulk NP solution, (iii) solvent evaporation, and (iv) recession of the three-phase interface. Below, we discuss how the NP film transformation (i.e., transition from colloidal gas to superlattice solid) is impacted by the sequence of these events.

The spreading of a liquid across the interface of an immiscible liquid subphase is driven by the Marangoni effect, a surface tension gradient, and related distortion created by the three-phase contact line. The spreading can be parameterized by the interfacial energetics, quantified by the spreading parameter (S)

$$S = \gamma_{0,2} - (\gamma_{0,1} + \gamma_{1,2}) \tag{1}$$

where γ are the surface or interface tensions, and 0, 1, and 2 represent the air, top phase (i.e., DE, ME, or DCB), and bottom phase (i.e., EG), respectively. 30 Spreading occurs if S >0, which means that the system can lower its energy by replacing the initial high-energy interface $(\gamma_{0,2})$ with a thin film with lower overall interfacial energy $(\gamma_{0,1} + \gamma_{1,2})$. That the rapid initial spreading of the NP monolayer (ML) is comparable for all three solvents indicates that the film formation is energetically favored in each case. The NP ML precursor film covers the trough in ~0.15 s after the addition of the NP solution to the top of the EG surface (see the videos in the Supporting Information). The rapid spreading at the rate of \sim 100 mm/s suggests a spreading force on the order of 10 mN/ m, 55 which is in line with the estimates based on the interfacial tension reported using hexane or toluene.⁵⁶ The surface tension is not expected to change significantly in the presence of NCs due to the similar chemical nature, and hence the spreading properties are expected to remain advantageous throughout the process. Given that the spreading of the NP ML precursor film is comparable and complete in each solvent case, we can conclude that the observed differences in the NP film morphology arise from processes that follow the initial spreading of the precursor film.

We can rationalize the different spreading behaviors observed for DE, ME, and DCB solutions in the context of the spreading energetics (eq 1) and the coupled dynamic processes of the NP superlattice formation and solvent evaporation. The key steps are schematically summarized in Figure S13. Concurrent with the spreading of the bulk solution, the colloidal NP concentration increases due to solvent evaporation (and miscibility in the case of DCB); the rate of concentration increase is a function of the distance from the injection site, being dependent on the local film thickness and liquid mass flow, and the more homogeneous evaporation rate. As the solution reaches the "solubility limit", the critical volume fraction at a given spot, the NP solution transforms

from a colloidal fluid into an initially solvated, later dry superlattice. In this comparison, we can ignore the effect of supersaturation and instead focus on a relative comparison of the solubilities for the three solvent classes investigated. Notably, the relative saturation concentration scales as DE > ME > DCB. The lower relative saturation concentration of NP dissolved in ME compared to that in DE explains why the bulk ME solution does not fully spread to the edge of the trough (i.e., it does not spread as far as the DE). As shown in Figure S12, the ME solution reaches supersaturation, which leads to the formation of the NP SL at the three-phase interface. The nascent SL formed at the interface pins the spreading of the bulk solution. With further solvent evaporation, the SL formation then propagates radially inward from the pinned interface, leaving behind a rather homogeneous, flat film with a thickness and morphology determined by the local nucleation and crystal growth processes.

The difference in the observed SL grain sizes can also be rationalized by comparing the saturation concentration in different solvents. Ceteris paribus, the superlattice nucleation rate scales approximately exponentially with the supersaturation of the colloidal solution,⁵⁷ which explains that ME and DCB solutions form smaller SL grains (higher nucleation rate) compared to DE solutions. Moreover, large oversaturation through rapid solvent loss and low solubility enhances the chances of vitrification (Kirkwood–Alder transition) or homogeneous nucleation leading to misoriented crystals, which could explain the disordered phase-scattering ring observed for DCB.

In summary, the discussion above provides new insights into the delicate choice of solvent for the NP solution wetting and SL film formation. The withdrawing droplet permanently loses NPs and volume, and a fine balance of evaporation rate and saturation concentration is required to achieve large-scale homogeneity. It is clear that ME is not an ideal solvent, as the edges of the droplet dry before the bulk droplet completely spreads (and a monolayer ring surrounds the rest of the film). The bulk ME solution thus remains in the form of droplets; both effects are caused by a low saturation concentration. The high-quality SL formed from DE solutions derives from the fact that the bulk solution spreads completely to form a largescale, homogeneous, flat film covering the entire trough. Through this example and the discussion, we can set the requirements for homogeneous film formation at liquid-liquid interfaces. The three, equally important properties of a suitable solvent are (1) low surface tension and high interfacial tension against the subphase to ensure complete wetting, (2) complete immiscibility with the subphase to limit solvent loss and set it controllable to avoid vitrification, and (3) excellent solubility for the NPs, allowing for crystallization at very high concentrations. Alkanes with strong affinity to the typical oleic acid ligands and low surface tension providing good wetting are ideal candidates, which explains the popularity of hexane and octane in similar studies. In our experiments, we observed that DE satisfies the conditions, and uniform superlattices are formed at a 10 cm² scale. The superlattice uniformity shown in the TEM images and the scattering data confirm that bulk crystallization is effectively avoided at this time scale. The final film thickness before drying (estimated to be around 100 nm, 5 times the estimated dry thickness) is enough to confine the crystallization to two dimensions. Nevertheless, we do see a decreasing thickness near the center of the trough; one will likely be able to overcome this issue by

optimizing the evaporation rate, the surface tension gradient at the edges of the drying droplet, and the solution viscosity.

CONCLUSIONS

In summary, we provide new insights into the physicochemical processes accompanying the formation of NP superlattices at the interface of two immiscible fluids. We examined how the interplay of surface tension-driven wetting and spreading and solvent evaporation-driven dewetting impacts the morphology of the self-assembled NP assemblies. The combination of in situ X-ray scattering and TEM provides both qualitative trends and detailed quantitative insights into the 2D superlattice assembly. Our comparison of three NP solvents (DE, ME, and DCB) illustrates that the solvent choice influences the nanoscopic softness of the colloidal NP shell, as well as the macroscopic fluid spreading behavior. We identified the NP solubility as a crucial factor in the formation of homogeneous, high-quality films. We observe that the precursor (i.e., NP monolayer) film spreading ahead of the droplet affects the final droplet size. In the case of "bad" solvents, the NPs bonding in the precursor film hinder the consecutive spreading of the bulk solution, while good solvents with high solubility (such as decane) are able to form a homogeneous film over a large area. During evaporation of the solvent, the interaction of the solvent with the particles, and not with the liquid substrate, affects the film morphology. On the other hand, the symmetry of the superlattice does not depend on the solvent, showing the robustness of the interparticle forces at the nanometer length scales. We expect that better understanding of the dynamics of the self-assembly process will help improve the methods used for large-scale, ordered NP superlattices and related metamaterials.

ASSOCIATED CONTENT

Solution Supporting Information

The Supporting Information is available free of charge at https://pubs.acs.org/doi/10.1021/acs.langmuir.0c00524.

Experimental and data processing details, and further discussion (PDF)

M1_decane (AVI)

M2_decane spreading (MP4)

M3 mesitylene (AVI)

M5_dichlorobenzene (AVI)

M4_mesitylene spreading (MP4)

M6_dichlorobenzene spreading (MP4)

AUTHOR INFORMATION

Corresponding Author

Tobias Hanrath — Robert F. Smith School of Chemical and Biomolecular Engineering, Cornell University, Ithaca, New York 14853, United States; ○ orcid.org/0000-0001-5782-4666; Email: th358@cornell.edu

Authors

Daniel M. Balazs — Robert F. Smith School of Chemical and Biomolecular Engineering, Cornell University, Ithaca, New York 14853, United States; orcid.org/0000-0001-7597-043X

Tyler A. Dunbar − Robert F. Smith School of Chemical and Biomolecular Engineering, Cornell University, Ithaca, New York 14853, United States; oorcid.org/0000-0003-2971-5766

Detlef-M. Smilgies – Robert F. Smith School of Chemical and Biomolecular Engineering and Cornell High Energy Synchrotron

Source (CHESS), Cornell University, Ithaca, New York 14853, United States; orcid.org/0000-0001-9351-581X

Complete contact information is available at: https://pubs.acs.org/10.1021/acs.langmuir.0c00524

Author Contributions

D.M.B. and T.A.D. contributed equally. The manuscript was written through contributions of all authors. All authors have given approval to the final version of the manuscript.

Notes

The authors declare no competing financial interest.

ACKNOWLEDGMENTS

This work was supported by the U.S. Department of Energy through award DE-SC0018026 and by the Cornell Center for Materials Research with funding from the NSF MRSEC program (DMR-1719875). Measurements were conducted at the Cornell High Energy Synchrotron Source (CHESS), which is supported by the National Science Foundation under award DMR-1332208.

REFERENCES

- (1) Whitesides, G. M.; Grzybowski, B. Self-Assembly at All Scales. *Science* **2002**, 295, 2418–2421.
- (2) Nie, Z.; Petukhova, A.; Kumacheva, E. Properties and Emerging Applications of Self-Assembled Structures Made from Inorganic Nanoparticles. *Nat. Nanotechnol.* **2010**, *5*, 15–25.
- (3) Boles, M. A.; Engel, M.; Talapin, D. V. Self-Assembly of Colloidal Nanocrystals: From Intricate Structures to Functional Materials. *Chem. Rev.* **2016**, *116*, 11220–11289.
- (4) Glotzer, S. C.; Solomon, M. J.; Kotov, N. A. Self-Assembly: From Nanoscale to Microscale Colloids. *AIChE J.* **2004**, *50*, 2978–2985.
- (5) Kovalenko, M. V.; Manna, L.; Cabot, A.; Hens, Z.; Talapin, D. V.; Kagan, C. R.; Klimov, V. I.; Rogach, A. L.; Reiss, P.; Milliron, D. J.; Guyot-Sionnnest, P.; Konstantatos, G.; Parak, W. J.; Hyeon, T.; Korgel, B. A.; Murray, C. B.; Heiss, W. Prospects of Nanoscience with Nanocrystals. *ACS Nano* **2015**, *9*, 1012–1057.
- (6) Zhou, Z.-Y.; Tian, N.; Li, J.-T.; Broadwell, I.; Sun, S.-G. Nanomaterials of High Surface Energy with Exceptional Properties in Catalysis and Energy Storage. *Chem. Soc. Rev.* **2011**, *40*, 4167–4185.
- (7) Crabtree, G. W.; Sarrao, J. L. Opportunities for Mesoscale Science. MRS Bull. 2012, 37, 1079–1088.
- (8) Henry, C. R. 2D-Arrays of Nanoparticles as Model Catalysts. *Catal. Lett.* **2015**, *145*, 731–749.
- (9) Kagan, C. R.; Lifshitz, E.; Sargent, E. H.; Talapin, D. V. Building Devices from Colloidal Quantum Dots. *Science* **2016**, 353, No. aac5523.
- (10) Talapin, D. V.; Lee, J.-S.; Kovalenko, M. V.; Shevchenko, E. V. Prospects of Colloidal Nanocrystals for Electronic and Optoelectronic Applications. *Chem. Rev.* **2010**, *110*, 389–458.
- (11) Vineis, C. J.; Shakouri, A.; Majumdar, A.; Kanatzidis, M. G. Nanostructured Thermoelectrics: Big Efficiency Gains from Small Features. *Adv. Mater.* **2010**, *22*, 3970–3980.
- (12) Urban, J. J. Prospects for Thermoelectricity in Quantum Dot Hybrid Arrays. *Nat. Nanotechnol.* **2015**, *10*, 997–1001.
- (13) Sun, S.; Murray, C. B.; Weller, D.; Folks, L.; Moser, A. Monodisperse FePt Nanoparticles and Ferromagnetic FePt Nanocrystal Superlattices. *Science* **2000**, 287, 1989–1992.
- (14) Nozik, A. J.; Beard, M. C.; Luther, J. M.; Law, M.; Ellingson, R. J.; Johnson, J. C. Semiconductor Quantum Dots and Quantum Dot Arrays and Applications of Multiple Exciton Generation to Third-Generation Photovoltaic Solar Cells. *Chem. Rev.* **2010**, *110*, 6873–6890
- (15) Baxter, J.; Bian, Z.; Chen, G.; Danielson, D.; Dresselhaus, M. S.; Fedorov, A. G.; Fisher, T. S.; Jones, C. W.; Maginn, E.; Kortshagen, U.; Manthiram, A.; Nozik, A.; Rolison, D. R.; Sands, T.; Shi, L.; Sholl,

- D.; Wu, Y. Nanoscale Design to Enable the Revolution in Renewable Energy. *Energy Environ. Sci.* **2009**, *2*, 559–588.
- (16) Min, Y.; Akbulut, M.; Kristiansen, K.; Golan, Y.; Israelachvili, J. The Role of Interparticle and External Forces in Nanoparticle Assembly. *Nat. Mater.* **2008**, *7*, 527–538.
- (17) Bishop, K. J. M.; Wilmer, C. E.; Soh, S.; Grzybowski, B. A. Nanoscale Forces and Their Uses in Self-Assembly. *Small* **2009**, *5*, 1600–1630.
- (18) Batista, C. A. S.; Larson, R. G.; Kotov, N. A. Nonadditivity of Nanoparticle Interactions. *Science* **2015**, *350*, No. 1242477.
- (19) Bigioni, T. P.; Lin, X.-M.; Nguyen, T. T.; Corwin, E. I.; Witten, T. A.; Jaeger, H. M. Kinetically Driven Self Assembly of Highly Ordered Nanoparticle Monolayers. *Nat. Mater.* **2006**, *5*, 265.
- (20) Bresme, F.; Oettel, M. Nanoparticles at Fluid Interfaces. J. Phys.: Condens. Matter 2007, 19, No. 413101.
- (21) Garbin, V.; Crocker, J. C.; Stebe, K. J. Nanoparticles at Fluid Interfaces: Exploiting Capping Ligands to Control Adsorption, Stability and Dynamics. *J. Colloid Interface Sci.* **2012**, 387, 1–11.
- (22) Evers, W. H.; Goris, B.; Bals, S.; Casavola, M.; de Graaf, J.; van Roij, R.; Dijkstra, M.; Vanmaekelbergh, D. Low-Dimensional Semiconductor Superlattices Formed by Geometric Control over Nanocrystal Attachment. *Nano Lett.* **2013**, *13*, 2317–2323.
- (23) Boneschanscher, M. P.; Evers, W. H.; Geuchies, J. J.; Altantzis, T.; Goris, B.; Rabouw, F. T.; van Rossum, S. A.; van der Zant, H. S. J.; Siebbeles, L. D. A.; Van Tendeloo, G.; Swart, I.; Hilhorst, J.; Petukhov, A. V.; Bals, S.; Vanmaekelbergh, D. Long-Range Orientation and Atomic Attachment of Nanocrystals in 2D Honeycomb Superlattices. *Science* **2014**, *344*, 1377–1380.
- (24) Whitham, K.; Yang, J.; Savitzky, B. H.; Kourkoutis, L. F.; Wise, F.; Hanrath, T. Charge Transport and Localization in Atomically Coherent Quantum Dot Solids. *Nat. Mater.* **2016**, *15*, 557–563.
- (25) Balazs, D. M.; Loi, M. A. Lead-Chalcogenide Colloidal-Quantum-Dot Solids: Novel Assembly Methods, Electronic Structure Control, and Application Prospects. *Adv. Mater.* **2018**, *30*, No. 1800082.
- (26) Dabbousi, B. O.; Murray, C. B.; Rubner, M. F.; Bawendi, M. G. Langmuir-Blodgett Manipulation of Size-Selected CdSe Nanocrystallites. *Chem. Mater.* **1994**, *6*, 216–219.
- (27) Santhanam, V.; Liu, J.; Agarwal, R.; Andres, R. P. Self-Assembly of Uniform Monolayer Arrays of Nanoparticles. *Langmuir* **2003**, *19*, 7881–7887.
- (28) Wen, T.; Majetich, S. A. Ultra-Large-Area Self-Assembled Monolayers of Nanoparticles. ACS Nano 2011, 5, 8868–8876.
- (29) Vegso, K.; Siffalovic, P.; Jergel, M.; Weis, M.; Benkovicova, M.; Majkova, E.; Luby, S.; Kocsis, T.; Capek, I. Silver Nanoparticle Monolayer-to-Bilayer Transition at the Air/Water Interface as Studied by the GISAXS Technique: Application of a New Paracrystal Model. *Langmuir* 2012, 28, 9395–9404.
- (30) de Gennes, P. G. Wetting: Statics and Dynamics. *Rev. Mod. Phys.* **1985**, *57*, 827–863.
- (31) Yu, W. W.; Falkner, J. C.; Shih, B. S.; Colvin, V. L. Preparation and Characterization of Monodisperse PbSe Semiconductor Nanocrystals in a Noncoordinating Solvent. *Chem. Mater.* **2004**, *16*, 3318–3322.
- (32) Moreels, I.; Lambert, K.; Muynck, D. D.; Vanhaecke, F.; Poelman, D.; Martins, J. C.; Allan, G.; Hens, Z. Composition and Size-Dependent Extinction Coefficient of Colloidal PbSe Quantum Dots. *Chem. Mater.* **2007**, *19*, 6101–6106.
- (33) Jiang, Z. GIXSGUI: A MATLAB Toolbox for Grazing-Incidence X-Ray Scattering Data Visualization and Reduction, and Indexing of Buried Three-Dimensional Periodic Nanostructured Films. J. Appl. Crystallogr. 2015, 48, 917–926.
- (34) Baxter, R. J. Percus-Yevick Equation for Hard Spheres with Surface Adhesion. *J. Chem. Phys.* **1968**, *49*, 2770–2774.
- (35) De Kruif, C. G.; Rouw, P. W.; Briels, W. J.; Duits, M. H. G.; Vrij, A.; May, R. P. Adhesive Hard-Sphere Colloidal Dispersions. A Small-Angle Neutron-Scattering Study of Stickiness and the Structure Factor. *Langmuir* 1989, *5*, 422–428.

- (36) Hansen, C. M. Hansen Solubility Parameters: A User's Handbook, 2nd ed.; CRC Press: Boca Raton, 2007.
- (37) Williamson, C. B.; Nevers, D. R.; Hanrath, T.; Robinson, R. D. Prodigious Effects of Concentration Intensification on Nanoparticle Synthesis: A High-Quality, Scalable Approach. *J. Am. Chem. Soc.* **2015**, *137*, 15843–15851.
- (38) Doblas, D.; Kister, T.; Cano-Bonilla, M.; González-García, L.; Kraus, T. Colloidal Solubility and Agglomeration of Apolar Nanoparticles in Different Solvents. *Nano Lett.* **2019**, *19*, 5246–5252.
- (39) Afsar-Siddiqui, A. B.; Luckham, P. F.; Matar, O. K. The Spreading of Surfactant Solutions on Thin Liquid Films. *Adv. Colloid Interface Sci.* **2003**, *106*, 183–236.
- (40) McBain, J. W.; Ford, T. F.; Wilson, D. A. Neue Methoden zum Studium der Oberflächen gewöhnlicher Lösungen. *Kolloid-Z.* **1937**, 78, 1–9.
- (41) Zisman, W. A. The Spreading of Oils on Water Part II. Non-Ionized Molecules Having Only One Polar Group. *J. Chem. Phys.* **1941**, *9*, 729–741.
- (42) Sawyer, W. M.; Fowkes, F. M. Monolayers in Equilibrium with Lenses of Oil on Water. I. Octadecanol and Tetradecanoic Acid in White Oil. *J. Phys. Chem. A.* **1956**, *60*, 1235–1239.
- (43) Smilgies, D.-M.; Heitsch, A. T.; Korgel, B. A. Stacking of Hexagonal Nanocrystal Layers during Langmuir–Blodgett Deposition. *J. Phys. Chem. B* **2012**, *116*, 6017–6026.
- (44) Ashcroft, N. W.; Lekner, J. Structure and Resistivity of Liquid Metals. *Phys. Rev.* **1966**, *145*, 83–90.
- (45) Bian, K.; Choi, J. J.; Kaushik, A.; Clancy, P.; Smilgies, D.-M.; Hanrath, T. Shape-Anisotropy Driven Symmetry Transformations in Nanocrystal Superlattice Polymorphs. *ACS Nano* **2011**, *5*, 2815–2823.
- (46) Weidman, M. C.; Smilgies, D. M.; Tisdale, W. A. Kinetics of the Self-Assembly of Nanocrystal Superlattices Measured by Real-Time in Situ X-Ray Scattering. *Nat. Mater.* **2016**, *15*, 775–781.
- (47) Abelson, A.; Qian, C.; Salk, T.; Luan, Z.; Fu, K.; Zheng, J.-G.; Wardini, J. L.; Law, M. Collective Topo-Epitaxy in the Self-Assembly of a 3D Quantum Dot Superlattice. *Nat. Mater.* **2020**, 49–55.
- (48) Xiong, S.; Dunphy, D. R.; Wilkinson, D. C.; Jiang, Z.; Strzalka, J.; Wang, J.; Su, Y.; de Pablo, J. J.; Brinker, C. J. Revealing the Interfacial Self-Assembly Pathway of Large-Scale, Highly-Ordered, Nanoparticle/Polymer Monolayer Arrays at an Air/Water Interface. *Nano Lett.* **2013**, *13*, 1041–1046.
- (49) Menon, S. V. G.; Manohar, C.; Rao, K. S. A New Interpretation of the Sticky Hard Sphere Model. *J. Chem. Phys.* **1991**, *95*, 9186–9190.
- (50) Binks, B. P.; Lumsdon, S. O. Influence of Particle Wettability on the Type and Stability of Surfactant-Free Emulsions. *Langmuir* **2000**, *16*, 8622–8631.
- (51) Lin, Y.; Skaff, H.; Emrick, T.; Dinsmore, A. D.; Russell, T. P. Nanoparticle Assembly and Transport at Liquid-Liquid Interfaces. *Science* **2003**, 299, 226–229.
- (52) McConnell, G. A.; Gast, A. P.; Huang, J. S.; Smith, S. D. Disorder-Order Transitions in Soft Sphere Polymer Micelles. *Phys. Rev. Lett.* **1993**, *71*, 2102–2105.
- (53) Pusey, P. N.; van Megen, W. Phase Behaviour of Concentrated Suspensions of Nearly Hard Colloidal Spheres. *Nature* **1986**, 320, 340–342.
- (54) Fan, Z.; Grünwald, M. Orientational Order in Self-Assembled Nanocrystal Superlattices. J. Am. Chem. Soc. 2019, 141, 1980–1988.
- (55) Fraaije, J. G. E. M.; Cazabat, A. M. Dynamics of Spreading on a Liquid Substrate. *J. Colloid Interface Sci.* **1989**, 133, 452–460.
- (56) Geuchies, J. J.; Soligno, G.; Geraffy, E.; Hendrikx, C. P.; van Overbeek, C.; Montanarella, F.; Slot, M. R.; Konovalov, O. V.; Petukhov, A. V.; Vanmaekelbergh, D. Unravelling Three-Dimensional Adsorption Geometries of PbSe Nanocrystal Monolayers at a Liquid-Air Interface. *Commun. Chem.* **2020**, *3*, No. 28.
- (57) Sear, R. P. Nucleation: Theory and Applications to Protein Solutions and Colloidal Suspensions. *J. Phys.: Condens. Matter* **2007**, *19*, No. 033101.